The Astrophysical Journal, 981:71 (10pp), 2025 March 1 https://doi.org/10.3847/1538-4357/adb0c7
© 2025. The Author(s). Published by the American Astronomical Society.
OPEN ACCESS

The Assembly of Supermassive Black Holes at $z < 1$ in Early-type Galaxies from Scaling Relations

D. Farrah[1,2], A. Engholm[1,2], E. Hatziminaoglou[3,4,5], S. Petty[6], F. Shankar[7], A. Efstathiou[8], K. Ejercito[1,2], K. Jones[1], M. Lacy[9], C. Lonsdale[9], C. Pearson[10,11,12], G. Tarlé[13], R. A. Windhorst[14], J. Afonso[15,16], D. L. Clements[17], K. S. Croker[1,14], and L. K. Pitchford[18,19]

[1] Department of Physics and Astronomy, University of Hawai'i at Mānoa, 2505 Correa Rd., Honolulu, HI 96822, USA; dfarrah@hawaii.edu
[2] Institute for Astronomy, University of Hawai'i, 2680 Woodlawn Dr., Honolulu, HI 96822, USA
[3] European Southern Observatory, Karl-Schwarzschild-Str. 2, 85748 Garching bei München, Germany
[4] Instituto de Astrofisica de Canarias (IAC), E-38205 La Laguna, Tenerife, Spain
[5] Universidad de La Laguna, Opto. Astrofisica, E-38206 La Laguna, Tenerife, Spain
[6] NorthWest Research Associates, 3380 Mitchell Ln., Boulder, CO 80301, USA
[7] Department of Physics and Astronomy, University of Southampton, Highfield SO17 1BJ, UK
[8] School of Sciences, European University Cyprus, Diogenes St., Engomi, 1516 Nicosia, Cyprus
[9] National Radio Astronomy Observatory, Charlottesville, VA, USA
[10] RAL Space, STFC Rutherford Appleton Laboratory, Didcot, Oxfordshire OX11 0QX, UK
[11] The Open University, Milton Keynes MK7 6AA, UK
[12] Oxford Astrophysics, University of Oxford, Keble Rd., Oxford OX1 3RH, UK
[13] Department of Physics, University of Michigan, 450 Church St., Ann Arbor, MI 48109, USA
[14] School of Earth and Space Exploration, Arizona State University, Tempe, AZ 85287-6004, USA
[15] Instituto de Astrofísica e Ciências do Espaço, Universidade de Lisboa, Portugal
[16] Departamento de Física, Faculdade de Ciências, Universidade de Lisboa, Portugal
[17] Imperial College London, Blackett Laboratory, Prince Consort Rd., London SW7 2AZ, UK
[18] Department of Physics and Astronomy, Texas A&M University, College Station, TX, USA
[19] George & Cynthia Woods Mitchell Institute for Fundamental Physics and Astronomy, Texas A&M University, College Station, TX, USA
Received 2024 August 25; revised 2025 January 22; accepted 2025 January 24; published 2025 February 27

Abstract

The assembly of supermassive black hole (SMBH) mass ($M_\bullet$) and stellar mass (M_*) in galaxies can be studied via the redshift evolution of the $M_\bullet$–M_* relation, but the ways in which selection bias and physical assembly channels affect this evolution are uncertain. To address this, we compare the $M_\bullet$–M_* relation for local massive ($M_* > 10^{10.5}\ M_\odot$) quiescent early-type galaxies (ETGs) to that for massive ETGs hosting active galactic nuclei (AGN) at $z \sim 0.8$. The restrictions on stellar mass and galaxy type limit the assembly channels that may connect the two relations. For the local sample we find $\log(M_\bullet) = 8.80 + 1.10(\log M_* - 11)$, in line with prior work. For the $z \sim 0.8$ sample we find a bias-corrected relation: $\log(M_\bullet) = 7.80 + 1.25(\log M_* - 11)$. We show, however, that this relation depends on the stellar and SMBH mass functions used to compute the selection bias, the virial relation, the virial factor, and the active fraction, which together introduce uncertainty of up to ∼0.6 dex in the $z \sim 0.8$ relation. Adopting reasonable choices of these parameters then our $z \sim 0.8$ relation lies above that for $z \sim 0$ AGN by ∼0.5 dex, but below our $z \sim 0$ ETG relation by 0.4–1 dex in SMBH mass. We discuss possible sources of this offset, including further bias corrections, "downsizing" in SMBH mass assembly, and preferential SMBH growth. Our results highlight the need to reduce uncertainties from selection and measurement bias in SMBH and stellar masses at all redshifts.

Unified Astronomy Thesaurus concepts: Black holes (162)

1. Introduction

Among galaxies at $z \sim 0$, scaling relations exist between supermassive black hole (SMBH) mass and some properties of their host galaxies (L. Ferrarese & D. Merritt 2000; K. Gebhardt et al. 2000; J. Kormendy & L. C. Ho 2013; N. J. McConnell & C.-P. Ma 2013; Y. Zhao et al. 2021). Potential origins of these scaling relations include feedback between the SMBH and star formation in its host galaxy (A. C. Fabian 2012; J. Silk 2013; R. Weinberger et al. 2017), a common fuel reservoir for SMBH accretion and star formation (e.g., Q. Ni et al. 2021), and galaxy–galaxy mergers (e.g., M. Hirschmann et al. 2010).

Studies of the evolution of galaxy scaling relations with redshift can, in principle, diagnose the processes that generate them. To date however, studies of this redshift evolution have produced conflicting results. Some find relatively more massive SMBHs at higher redshift (R. Decarli et al. 2010; A. Merloni et al. 2010; X. Ding et al. 2020; Y. Zhang et al. 2023). Others find more massive SMBHs at lower redshifts (Y. Ueda et al. 2018), or no clear evidence for evolution (M. Schramm & J. D. Silverman 2013; H. Suh et al. 2020; J. I. H. Li et al. 2021b; A. P. Cloonan et al. 2024; T. S. Tanaka et al. 2025). The origin of these discrepancies may lie in one or more of selection bias, measurement bias, and physical mass change channels.

Progress on determining which factors influence the redshift evolution of galaxy scaling relations can be made by restricting studies to specific galaxy types, since this limits the processes that must be considered. Early-type galaxies (ETGs) at $z < 1$ with total stellar masses $M_* \gtrsim 10^{10.5}\ M_\odot$ are suited to this

Original content from this work may be used under the terms of the Creative Commons Attribution 4.0 licence. Any further distribution of this work must maintain attribution to the author(s) and the title of the work, journal citation and DOI.

Table 1
Additional Low-redshift Early-type Galaxies (Section 2)

Name	z	$M_\bullet$	M_*
		($\log M_\odot$)	
A1201	0.169	$10.52^{+0.09}_{-0.11}$	12.25 ± 0.30
UGC 2698	0.021	$9.39^{+0.12}_{-0.17}$	11.56 ± 0.15
NGC 708	0.016	$10.00^{+0.11}_{-0.14}$	11.45 ± 0.30
NGC 1272	0.013	$9.70^{+0.20}_{-0.40}$	11.90 ± 0.30
NGC 2832	0.023	$9.77^{+0.13}_{-0.18}$	12.08 ± 0.30
NGC 3258	0.009	$9.35^{+0.05}_{-0.05}$	11.72 ± 0.30
NGC 4281	0.008	$8.69^{+0.02}_{-0.02}$	10.88 ± 0.50

References. J. W. Nightingale et al. (2023), J. H. Cohn et al. (2021), S. de Nicola et al. (2024), R. Saglia et al. (2024), J. E. Greene et al. (2019), B. D. Boizelle et al. (2019), and S. Thater et al. (2019).

purpose as they emerge en masse onto the red sequence at this epoch, on which they evolve fairly passively, and because the $M_\bullet$–M_* relation likely does not strongly deviate from a log-linear form at $M_* \gtrsim 10^{10.5}\ M_\odot$ (D. Sijacki et al. 2015; though see M. Habouzit et al. 2021). A recent study that took this approach (D. Farrah et al. 2023b, hereafter F23) compared the $M_\bullet$–M_* relation in local quiescent ETGs to that for active galactic nuclei (AGN) hosted in ETGs at $z \gtrsim 0.8$. They found evidence for relatively less massive SMBHs in ETGs at $z \sim 0.8$ compared to locally, by a factor of about 7. However, while F23 made bias corrections, their selection-bias correction was not based on a direct estimate from galaxy populations. They also used a novel method to compare the high- and low-redshift samples, via shifting populations in the ($M_\bullet$, M_*) plane, rather than the usual approach of deriving analytic scaling relations, which limited comparisons to prior works.

In this paper, we improve on the analysis in F23. We focus on two samples; a low-redshift ($z < 0.2$) quiescent ETG sample and a high-redshift ($z \sim 0.8$) sample of AGN in ETG hosts, selected to represent ETGs about to emerge onto the red sequence. We compare the $M_\bullet$–M_* relations of the two samples to each other to examine the assembly of ETGs since $z \sim 1$. In doing so, we explore the impact of different selection and measurement bias corrections. Section 2 presents the two samples. Section 3 describes the selection and measurement bias corrections. Section 4 presents our results, including the low-redshift $M_\bullet$–M_* relation, the high-redshift observed and intrinsic $M_\bullet$–M_* relations, and the processes that may align them. We discuss these results in Section 5 and present our conclusions in Section 6. We assume $H_0 = 70$ km s^{-1} Mpc^{-1}, $\Omega = 1$, and $\Omega_\Lambda = 0.7$. We convert literature data to this cosmology and a P. Kroupa (2002) initial mass function (IMF) where necessary. For ease of comparison with past work we use $\mu = \log_{10} M_\bullet$ and $s = \log_{10} M_*$. All uncertainties on derived parameters are 2σ (95%).

2. Sample Selection

To assemble the low-redshift sample, we start with the low-redshift ETGs in F23. Their selection criteria are an early-type morphology, a total stellar mass of $M_* > 10^{10.5}\ M_\odot$, an SMBH mass measured via stellar dynamical modeling, and no evidence for an AGN, pseudobulge, or bar. We exclude NGC 5018 as its dusty center may make stellar mass estimates difficult. We add seven objects that were either presented recently, or have an SMBH mass measured via gas dynamical modeling (Table 1) since gas and stellar dynamical modeling give similar SMBH masses (e.g., T. K. Waters et al. 2024). The final sample comprises 57 objects.

To assemble the high-redshift sample, we follow the procedure in F23. In F23, the Wide-field Infrared Survey Explorer–selected AGN catalog of R. S. Barrows et al. (2021) was merged with the Sloan Digital Sky Survey (SDSS) DR14 quasar catalog of S. Rakshit et al. (2020) to form the parent catalog. AGN were then selected with $0.8 < z < 0.9$, a total stellar mass of $M_* > 10^{10.5}\ M_\odot$, an ETG host spectral energy distribution (SED), AGN reddening of $E(B-V) < 0.2$, and star formation rates (SFRs) at least a factor of 3 below the SFR–M_* main sequence. The redshift range places the sample near the end of the emergence of the red sequence, and is low enough that the R. S. Barrows et al. (2021) catalog is reasonably complete in stellar mass to $M_* = 10^{10.5}\ M_\odot$. The narrow redshift range also means the sample can be treated as luminosity limited, which is necessary for the selection-bias correction in Section 3.2. We make two changes to the procedure in F23. First, we update to the Q. Wu & Y. Shen (2022) quasar catalog, which is based on SDSS DR16. The resulting sample is almost identical to that obtained using the S. Rakshit et al. (2020) catalog. Second, since the bias model in Section 3.2 assumes a luminosity-limited sample, we find the luminosity limit of the sample, $10^{45.5}$ erg s^{-1}, using the bolometric luminosities from R. S. Barrows et al. (2021) of all quasars at $0.8 < z < 0.9$ in Q. Wu & Y. Shen (2022). We remove the quasars below this limit, to leave a final sample of 287 objects. We do not consider the other high-redshift samples in F23, or other literature samples, as they lack the combination of homogeneous selection, a narrow redshift range, large sample size, and homogeneously measured AGN and host properties.

3. Bias Corrections

We aim to compare the intrinsic $M_\bullet$ to intrinsic M_* relation derived from the low-redshift sample to the same relation derived from the high-redshift sample immediately after their AGN phase completes and they settle into quiescence. This requires several bias corrections, which we detail below.

3.1. Preliminary Considerations

3.1.1. Accretion Bias

Since the high-redshift sample is within an AGN phase, SMBH growth via accretion before they transition to quiescence is inevitable, and must be accounted for. F23 do so by increasing the individual SMBH masses by an amount drawn from $\Delta \log M_\bullet = U(0, 0.1)$ (their Appendix B2). Here, our approach makes this accretion degenerate with other SMBH growth channels. So, we conservatively assume a fixed correction equal to the maximum in F23, of 0.1 dex.

3.1.2. Stellar Mass Biases

For the stellar masses of the low- and high-redshift samples, two corrections must be considered. First is measurement bias. Second is Eddington bias, in which systems with smaller stellar masses are more likely to scatter upwards due to measurement error, than are systems with larger stellar masses to scatter downwards.

Table 2
The Stellar Mass Function (Schechter) and Total Supermassive Black Hole Mass Function and Eddington Ratio Distribution Function (Modified Schechter and Schechter) Combinations

#	Φ^*	s^*	α_*	$\Phi^{2,*}$	$\alpha_{2,*}$	References	$\Phi^\bullet$	$\mu^\bullet$	$\alpha_\bullet$	$\beta_\bullet$	λ^λ	α_λ	References
1	−3.01	10.86	−1.37	⋯	⋯	M21 (single)	−4.88	8.06	−1.19	0.57	−1.02	−1.09	S15 (SDSS)
2	−2.67	10.51	0.08	−3.07	−1.49	M21 (double)	−4.88	8.06	−1.19	0.57	−1.02	−1.09	S15 (SDSS)
3	−2.23	10.64	−0.52	⋯	⋯	W16	−4.88	8.06	−1.19	0.57	−1.02	−1.09	S15 (SDSS)
4	−5.96	10.89	−2.01	−3.02	−0.47	W23 (quiescent)	−4.88	8.06	−1.19	0.57	−1.02	−1.09	S15 (SDSS)
5	−3.08	11.02	−1.32	−3.18	−0.63	W23 (total)	−4.88	8.06	−1.19	0.57	−1.02	−1.09	S15 (SDSS)
6	−3.08	11.02	−1.32	−3.18	−0.63	W23 (total)	−5.32	9.09	−1.50	0.96	−1.19	−0.29	S15 (Comb.)

Note. Listed are the normalizations, break parameters (mass or Eddington ratio), and slope(s). The M21 stellar mass functions (SMFs) are their intrinsic $0.75 < z < 1.25$ versions. The W16 SMF is for $z \sim 0$ with specific SFRs of 10^{-11}–10^{-12} yr^{-1}. The W23 SMFs are for the 1.3 deg^2 COSMOS field at $0.8 < z < 1.1$. The total SMBH functions (BHMFs) and Eddington ratio distribution functions (ERDFs) from S15 are at $z \sim 0.8$. Set #1 is our default (Section 3.2).

For the low-redshift sample, we estimate the stellar measurement bias by comparing to the objects in common with A. E. Watkins et al. (2022), who estimate stellar masses via integrated 3.6 and 4.5 μm photometry. Their stellar masses are ∼0.1 dex lower than ours. Since it is unclear which of the measurement methods is closer to the truth, we do not apply a measurement bias correction. The level of Eddington bias in the low-redshift sample is also likely small, so for simplicity we do not correct for this either. We note, though, that applying either correction would increase the offset between the low- and high-redshift $M_\bullet$–M_* relations in Section 4.

For the high-redshift sample, measurement bias may arise because the stellar masses of the high- and low-redshift samples are measured in different ways: SED decomposition and near-infrared spatial profile fitting, respectively. This bias is, however, challenging to estimate. F23 find that measurement bias lowers the stellar masses of the high-redshift sample by 0.2–0.3 dex, though this could also arise from aligning two-dimensional inhomogeneous samples. J. I. H. Li et al. (2021b) find that stellar masses from SED decomposition are ∼0.1 dex lower than those from profile fitting, though their sample is not directly comparable to ours. A measurement bias of ∼0.1–0.2 dex low thus seems plausible, though a bias outside this range in either direction cannot be ruled out. The Eddington bias in the high-redshift sample is also difficult to estimate, as it will depend on the parameters in our selection-bias model (Section 4.2). Self-consistently investigating this bias is beyond the scope of this paper. However, we argue that the Eddington bias is small. Using the combinations of mass function parameters in Table 2 then this bias is negligible at $M_* \lesssim 10^{10.7}\,M_\odot$, rising to 0.1–0.2 dex at $M_* \sim 10^{11.5}\,M_\odot$. The measurement bias and the Eddington bias for the high-redshift samples are thus of comparable magnitude but opposite sign. We therefore make the simplifying assumption that these corrections cancel each other, and so do not apply either. We note that the magnitude of either is smaller than the uncertainty in the selection-bias correction (Section 4.2).

3.1.3. Supermassive Black Hole Measurement Bias

The SMBH masses of the two samples are measured using different methods—dynamical modeling for the low-redshift sample, and Mg II λ2799 single-epoch virial (SEV) masses for the high-redshift sample. Following S. Thater et al. (2022), we assume negligible measurement bias in the low-redshift SMBH masses (though see S. Thater et al. 2023). For the high-redshift sample, there exist several SEV calibrations, which can differ by ∼0.3 dex. We adopt the Y. Shen et al. (2011, hereafter S11) calibration, as it is used to compute the SMBH mass functions in Section 3.2. The S11 relation has a scatter of $\sigma_V \simeq 0.4$ dex. We explore other SEV choices in Section 4.2.

3.2. Selection Bias

As they are AGN, the SMBH masses of the high-redshift sample may be biased high with respect to the SMBH population. In F23 this was accounted for via a correction drawn from $\Delta \log M_\bullet = U(-0.3, -0.1)$. We improve on this treatment by adopting the bias model of A. Schulze & L. Wisotzki (2011). The model assumes an intrinsic mean $M_\bullet$–M_* relation:

$$\mu = a + bs, \tag{1}$$

with scatter σ_i. If μ and s are lognormally distributed, then the probability of obtaining μ, given s, is:

$$g(\mu|s) = \frac{1}{\sqrt{2\pi}\,\sigma_i} \exp\left(\frac{(\mu - a - bs)^2}{2\sigma_i^2}\right). \tag{2}$$

Given an intrinsic SMF $\Phi_*(s)$, the BHMF $\Phi_{\bullet,\mathrm{tot}}(\mu)$, is:

$$\Phi_{\bullet,\mathrm{tot}}(\mu) = \int g(\mu|s)\Phi_*(s)ds. \tag{3}$$

The selection bias is quantified by comparing Equation (3) to the intrinsic active BHMF, $\Phi_{\bullet,\mathrm{act}}(\mu)$, itself moderated by selection biases in the sample relative to all active SMBHs. For a sample luminosity limited at L_{lim} the SMBH selection function, $\Omega(\mu)$, is:

$$\Omega(\mu) = p_{\mathrm{act}} \int_{L_{\mathrm{lim}}}^{\infty} p(L, \mu)dL, \tag{4}$$

in which p_{act} is the fraction of SMBHs that are active, and $p(L, \mu)$ is the probability of finding an SMBH at a point in the (L,μ) plane. The active fraction is:

$$p_{\mathrm{act}} = \frac{\Phi_{\bullet,\mathrm{act}}(\mu)}{\Phi_{\bullet,\mathrm{tot}}(\mu)}, \tag{5}$$

and $p(L, \mu)$ is:

$$p(L, \mu) = \frac{\Phi_\lambda(\lambda)}{\int \Phi_\lambda(\lambda)d\lambda}, \tag{6}$$

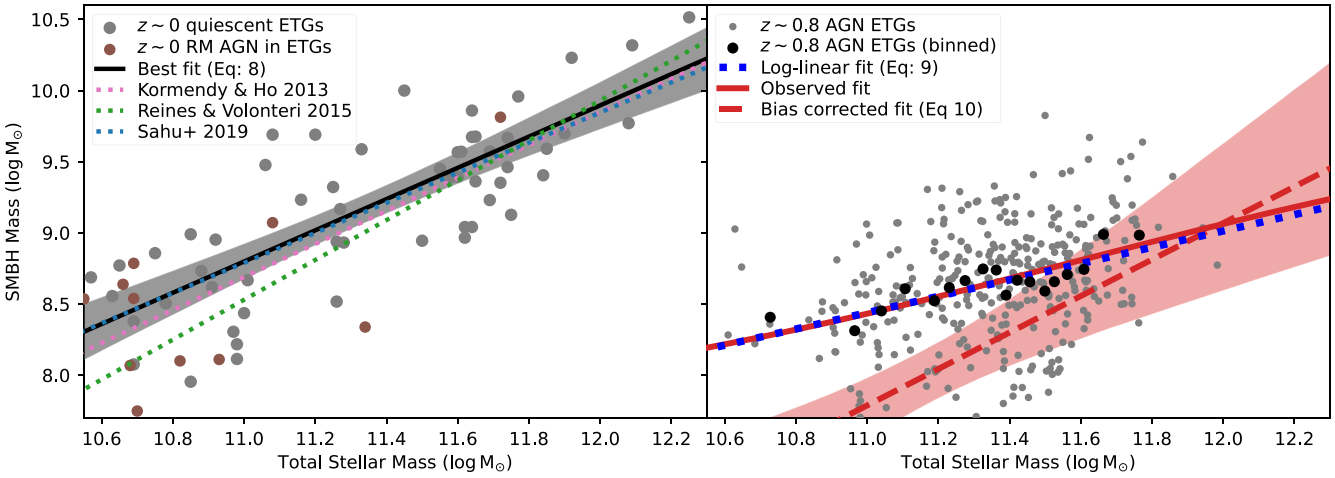


Figure 1. Left: The low-redshift sample in the $M_\bullet$–M_* plane with our best fit (Equation (8)). Also plotted are the relations for ETGs from J. Kormendy & L. C. Ho (2013), A. E. Reines & M. Volonteri (2015), and N. Sahu et al. (2019), and the compilation of AGN in ETG hosts at $z\sim0$ from F23. Right: the high-redshift sample in the $M_\bullet$–M_* plane with our log-linear fit (Equation (9)) and selection-bias-corrected fit (Equation (10)) and observed fits from the model in Section 3.2. The shaded regions are 2σ confidence intervals.

in which $\Phi_\lambda(\lambda)$ is the ERDF. The relation between stellar mass and observed SMBH mass is then:

$$\langle\mu\rangle(s) = \frac{\int \mu\Omega(\mu)g(\mu|s)d\mu}{\int\Omega(\mu)g(\mu|s)d\mu}, \quad (7)$$

in which $\langle\mu\rangle(s)$ is the mean of the logarithm of the SMBH masses, rather than the logarithm of their mean. The difference between Equations (7) and (1) is the selection bias in the sample.

Equation (7) requires the intrinsic SMF and the active BHMF and ERDF. We adopt functions from studies based on samples close to ours. For the SMF we use the single-Schechter intrinsic SMF at $0.75<z<1.25$ from D. J. McLeod et al. (2021, hereafter M21). This SMF is based on a near-infrared-selected sample from multiple fields spanning ~3 deg^2, and has good sampling of stellar masses at $>10^{11}$ $M_\odot$. Their use of a Chabrier IMF should not introduce significant bias as it is close to a Kroupa IMF. For the active BHMF and ERDF we adopt modified Schechter and Schechter forms, respectively, from A. Schulze et al. (2015, hereafter S15). Their ERDF assumes an $M_\bullet$-dependent break Eddington ratio (their Equations (15) and (16)). We select their "SDSS" parameters at $z\sim0.8$, since our sample is drawn from the SDSS. This parameter set is listed in Table 2.

The SMBH masses of the low-redshift sample may also be biased high, as the method used to measure them requires that the SMBH sphere of influence be resolved. For $M_*>10^{10.5}$ $M_\odot$ it has been argued that this bias is up to $\sim$0.4 dex (F. Shankar et al. 2016, 2020a; R. Carraro et al. 2020). We consider this possibility in Section 4.

4. Results

4.1. The Low- and High-redshift M$_\bullet$–M$_*$ Relations

We fit a function of the form in Equation (1) to the low-redshift sample.[20] This gave a mean relation:

$$\mu = 8.80^{+0.12}_{-0.12} + 1.10^{+0.21}_{-0.21}(s-11), \quad (8)$$

(Figure 1, left), with $\sigma_{\rm obs}=0.37^{+0.08}_{-0.06}$ (this includes intrinsic scatter, observational uncertainty, and scatter from calibration uncertainties in the stellar and SMBH masses). These results are in agreement with prior work (J. Kormendy & L. C. Ho 2013; A. E. Reines & M. Volonteri 2015; N. Sahu et al. 2019). As verification, we compare in Figure 1, left, to the compilation of AGN in ETG hosts at $z\sim0$ from F23 with SMBH masses from reverberation mapping and the Event Horizon Telescope. This compilation is also consistent with our fit.

For the high-redshift sample, we first give a direct comparison to the low-redshift sample by fitting a function of the form in Equation (1). This yields:

$$\mu = 8.46^{+0.08}_{-0.08} + 0.53^{+0.18}_{-0.17}(s-11), \quad (9)$$

(Figure 1, right), with $\sigma_{\rm obs}=0.39^{+0.04}_{-0.03}$. This scatter is comparable to that in the S11 relation. It is possible that the selection of our host galaxies as ETGs reduces this scatter, but we do not explore this further.

Next, we derive the intrinsic mean high-redshift $M_\bullet$–M_* relation by applying the selection-bias model in Section 3.2 to the high-redshift sample. To reduce computation time, we bin the sample in 18 bins of stellar mass, equally divided in object number. We then evaluate the log likelihood by comparing the predictions from Equation (7) to these binned data. We adopt parameter set #1 from Table 2 and the S11 SEV calibration. Since $p_{\rm act}$ can lie above unity for arbitrary choices of parameters in Equation (5), and because studies that constrain $p_{\rm act}$ are to some extent model dependent (R. Aversa et al. 2015; I. Delvecchio et al. 2020) we impose a loose constraint: $10^{-4}<p_{\rm act}<0.2$ at any $M_\bullet$. Since the scatter in Equation (1), σ_i, may be affected by the scatter in the SEV calibration, σ_V, we model the scatter in Equation (1) as $\sigma_i=\sqrt{\sigma_t^2+\sigma_V^2}$, where σ_t is the true intrinsic scatter.[21] The fit yields:

$$\mu = 7.80^{+0.18}_{-0.24} + 1.25^{+0.68}_{-0.47}(s-11), \quad (10)$$

[20] All model fitting was performed within Python 3.10.1, using Dynesty v2.1.2 (J. S. Speagle 2020), with a random seed of 1001.

[21] The scatter that goes into the log likelihood, σ_{ll}, is not the same as σ_i or σ_t–σ_{ll} does not enter Equation (2) or Equation (7). Instead, σ_{ll} is the scatter among the binned points in Figure 1, right and only appears in the log likelihood. It is found to be small: $\sigma_{ll}=0.11^{+0.02}_{-0.04}$.

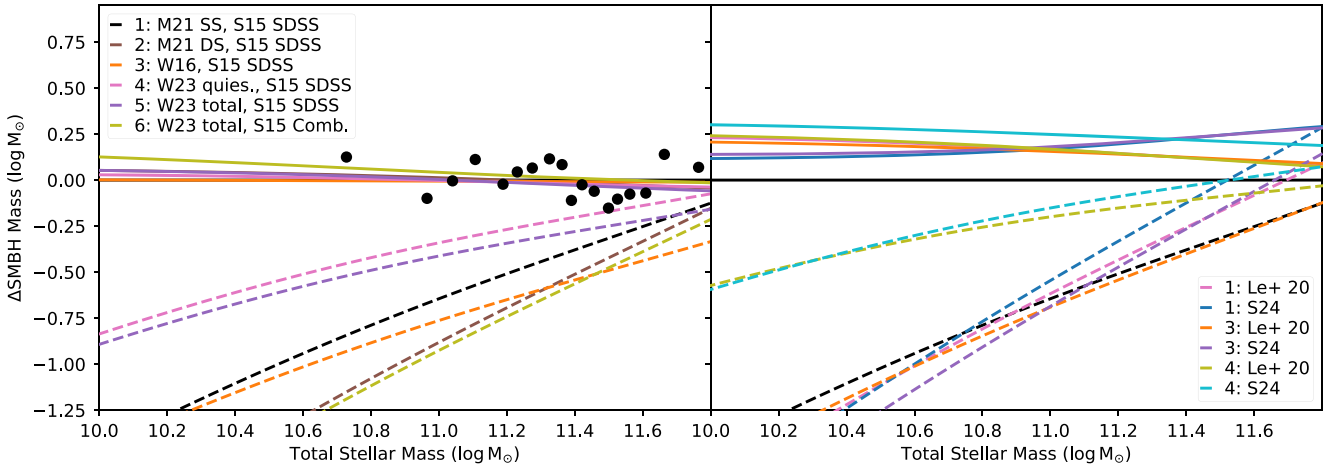


Figure 2. The impact on the high-redshift observed (solid) and intrinsic (dashed) fit of (left) the SMF, BHMF, and ERDF parameters (Table 2), and (right) the SEV calibrator (Section 4.2). The W. Zuo et al. (2015) results are close to the H. A. N. le et al. (2020) results and are omitted for clarity. In both panels, the fits are shown relative to the observed fit using parameter set #1. The data are not plotted in the right panel since they depend on the SEV calibrator.

(Figure 1, right), with $\sigma_t = 0.24^{+0.18}_{-0.38}$. The slope is consistent within 1σ with the slope in Equation (8). There is degeneracy between σ_t and both a and b; a Kendall-τ test yields $(\tau,\ p) = (-0.27,\ <0.01)$ and $(\tau,\ p) = (0.44,\ <0.01)$, respectively. The effects are, however, small—increasing σ_t by 0.2 decreases a by 0.08 and increases b by 0.25. Comparing Equation (10) to the observed mean relation (Equation (7)) implies stellar-mass-dependent selection bias in the sample. The level of bias is in agreement with other high-redshift luminous AGN (Y. Shen et al. 2008; A. Schulze & L. Wisotzki 2011).

4.2. Effect of Parameter Choices

We first consider the impact on the high-redshift selection-bias fit of the SMF, and active BHMF and ERDF. Our choice of parameter set #1 is based on the selection of the sample at $z \sim 0.8$ from SDSS fields. Since, however, these parameters are not measured for our sample in particular, other choices are possible. To explore the sensitivity of our results to this choice, we consider the following SMFs: the double-Schechter intrinsic SMF at $z \sim 0.8$ from M21, the quiescent and total SMFs at $z \sim 0.8$ from J. R. Weaver et al. (2023, hereafter W23), and the $z \sim 0$ SMF for quiescent SDSS galaxies from A. K. Weigel et al. (2016, hereafter W16). The W23 and W16 SMFs may not be as well matched to our sample as those from M21 as they are either constructed in smaller fields, or at lower redshift, but they should serve as comparisons. For the active BHMF and ERDF there are few studies in our redshift range, so we draw on S15 again, who present a "combined" BHMF/ERDF derived using several data sets, including the SDSS.

We fit our high-redshift sample with combinations of these SMFs, BHMFs, and ERDFs, but found limited preference for one over another. Replacing our default SMF with any of the alternative SMFs gave comparable quality fits. For the active BHMF/ERDF, the "SDSS" version gave better quality fits in most (but not all) cases. A selection of parameters that give acceptable fits is listed in Table 2 and plotted in Figure 2, left. While these combinations give comparable observed relations, they can give markedly different intrinsic relations. For example, using parameter set #4 gives:

$$\mu = 8.09^{+0.21}_{-0.20} + 0.95^{+0.42}_{-0.34}(s - 11), \quad (11)$$

with $\sigma_t = 0.09^{+0.25}_{-0.40}$.

We explored if our high-redshift sample can, in concert with the selection-bias model, constrain the SMF, BHMF, and ERDF. To do so, we allowed their parameters to vary with wide uniform priors. This yielded no useful constraints. We found $6.7 \lesssim a \lesssim 8.8$, $0.5 \lesssim b \lesssim 2.2$, and $\sigma_t < 1$. The single-Schechter SMF, BHMF, and ERDF parameters were constrained to lie within an order of magnitude of the parameter set #1 values.

Next, we examined the impact of adopting a different SEV calibration to that of S11. We considered three alternatives. W. Zuo et al. (2015) present a calibration for quasars at $z \sim 3.5$. H. A. N. le et al. (2020) consider a low-redshift sample over ~5 dex in luminosity. Y. Shen et al. (2024, hereafter, S24) present a relation based on the SDSS reverberation mapping program. A caveat to this analysis is that our adopted BHMFs/ERDFs are computed using the S11 calibrator. Changing the SEV calibrator will change the parameters of the BHMF/ERDF. Self-consistently recomputing the BHMF/ERDF for the alternative SEV calibrators is beyond the scope of this paper, so we take a simpler approach that should still be indicative. We increase (decrease) $\mu^*(\lambda(\lambda))$ by the average increase in the SMBH masses using the alternate SEV calibrators. For W. Zuo et al. (2015) and H. A. N. le et al. (2020) this is 0.15 dex, and for S24 this is 0.25 dex.

The results are shown in Figure 2, right. Different SEV calibrators can affect the derived intrinsic relation, even for the same SMF, BHMF, and ERDF. For example, using parameter set #1 with the S24 calibrator gives an intrinsic relation:

$$\mu = 7.90^{+0.19}_{-0.22} + 1.67^{+0.49}_{-0.51}(s - 11), \quad (12)$$

with $\sigma_t = 0.24^{+0.23}_{-0.38}$ (see Equation (10)). With parameter set #4 the S24 calibrator gives:

$$\mu = 8.29^{+0.17}_{-0.26} + 0.96^{+0.30}_{-0.40}(s - 11), \quad (13)$$

with $\sigma_t = 0.08^{+0.20}_{-0.25}$ (see Equation (11)).

Finally, motivated by the possibility that the intrinsic low-redshift $M_\bullet$–M_* relation is of log-polynomial form (F. Shankar et al. 2016), we test if the high-redshift intrinsic relation is of log-polynomial form. To do so, we modify Equations (1) and (2) to read:

$$\mu = a + bs - cs^2 - ds^3, \quad (14)$$

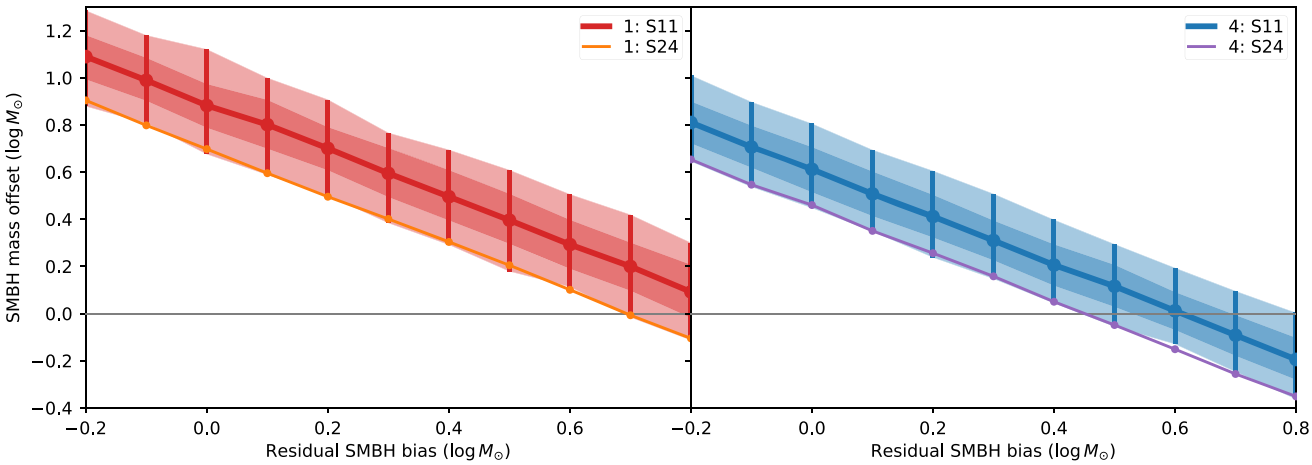


Figure 3. The SMBH mass offset needed to align the low- and intrinsic high-redshift relations for parameter sets #1 and #4, and the S11 and S24 SEV calibrators, as a function of residual SMBH mass bias (Section 4.3). The shaded regions show the 1σ and 2σ confidence intervals.

$$g(\mu|s) = \frac{1}{\sqrt{2\pi}\,\sigma_i} \exp\left(\frac{(\mu - a - bs + cs^2 + ds^3)^2}{2\sigma_i^2}\right), \quad (15)$$

respectively, and then fit for the coefficients in Equation (14). We found no significant change in fit quality. Coefficients a and b were consistent with their original values, though with larger errors. Coefficient c was consistent with zero, with large uncertainties. There was a hint that $d < 0$ but only at 2σ significance. We thus find no evidence preferring a log-polynomial relation, though we cannot rule it out.

4.3. Redshift Evolution of the M•–M$_*$ Relation

We here determine the offset in SMBH mass needed to align our high-redshift intrinsic $M_\bullet$–M_* relation with our low-redshift mean relation. To do so, we modify our analysis to draw the intrinsic slope of the high-redshift relation from the slope posterior of the low-redshift relation, rather than treating it as a free parameter. We then fit for the SMBH mass offset needed to align the relations using the selection-bias model in Section 3.2 and subsequent application of the accretion bias in Section 3.1.1. Since there may be "residual" SMBH bias arising from effects we have not corrected for, we perform several such fits, each for an amount of fixed residual SMBH bias between −0.2 and 0.8 dex. Following the results in Section 4.2, we restrict this analysis to parameter sets #1 and #4, and the S11 and S24 SEV calibrators.

The results are shown in Figure 3. With parameter set #1, the S11 (S24) SEV calibrator, and no residual SMBH mass bias the SMBH offset between the high- and low-redshift relations is $\Delta M_\bullet = 0.88^{+0.24}_{-0.21}$ dex, $\sigma = 0.17^{+0.21}_{-0.24}$ ($\Delta M_\bullet = 0.69^{+0.20}_{-0.16}$ dex, $\sigma = 0.11^{+0.20}_{-0.20}$). With parameter set #4 and the S11 (S24) SEV calibration we recover $\Delta M_\bullet = 0.61^{+0.20}_{-0.16}$ dex, $\sigma = 0.09^{+0.17}_{-0.13}$ ($\Delta M_\bullet = 0.46^{+0.28}_{-0.25}$ dex, $\sigma = 0.09^{+0.20}_{-0.13}$). There is degeneracy between $\Delta M_\bullet$ and σ—a Kendall-τ test yields $(\tau,\ p) = (0.12,\ <0.01)$—but the effect is small; reducing σ by 0.1 reduces $\Delta M_\bullet$ by ∼0.08. This degeneracy was also found by J. Li et al. (2021a).

Next, we replace an SMBH mass offset with cosmologically coupled black hole (BH) growth (V. Faraoni & A. Jacques 2007; K. S. Croker & J. L. Weiner 2019; K. S. Croker et al. 2022; M. Cadoni et al. 2023b). In such models, the mass of the BH increases with the cosmological scale factor, due to being embedded in an expanding universe (V. Faraoni & M. Rinaldi 2024). The initial and final BH mass are related by:

$$M_{\bullet,f} = M_{\bullet,i}\left(\frac{a_f}{a_i}\right)^k, \quad (16)$$

(K. S. Croker et al. 2020) where k is the coupling strength and a is the cosmological scale factor. Since we are now fitting for k, we modify our analysis as follows. For a given k, we individually shift the low-redshift objects to $z = 0$ and derive the resulting $M_\bullet$–M_* relation. We then shift the intrinsic high-redshift relation to $z = 0$ and compare it to the low-redshift relation. The results are shown in Figure 4. With set #1, the S11 (S24) SEV calibrator, and no residual SMBH bias, $k = 3.40^{+0.78}_{-0.82}$ ($k = 2.72^{+0.87}_{-0.56}$). With set #4, $k = 2.32^{+0.75}_{-0.57}$ ($k = 1.94^{+1.27}_{-0.99}$). The scatter is comparable to that found for the $\Delta M_\bullet$ fits, and we see the same, small, degeneracy: $(\tau,\ p) = (0.14,\ <0.01)$ (decreasing σ by 0.1 will change k by at most 0.5).

5. Discussion

5.1. Selection Bias in High-redshift Active Galactic Nuclei

The selection bias in the high-redshift sample depends on the SMF, BHMF, and ERDF. Different choices can give comparable observed relations, but intrinsic relations that differ by up to ∼0.4 in slope and ∼0.5 dex in intercept (Figure 2). The variations in the SMF, BHMF, and ERDF that give this range in the intrinsic relation are comparable to those seen between $\Delta z \sim 0.5$ intervals over $0 < z \lesssim 4$ (S15; M21; W23). Our results also show that constraints on the SMF, BHMF, and ERDF from samples of order 10^2 objects in the $M_\bullet$–M_* plane are challenging. Furthermore, the choice of SEV calibration can shift the intrinsic relation by ∼0.2 dex, and alter its slope (Figure 2).

There are two further sources of uncertainty. First is the virial factor, $f_{\rm vir}$, where SMBH masses from the virial method are computed via $M_\bullet = f_{\rm vir}(c\tau v^2/G)$, in which $c\tau$ is the time delay, v is the line velocity width, and G is Newton's constant. We have assumed $f_{\rm vir} = 4.3$, but this value is debated (J. E. Mejía-Restrepo et al. 2018). Some studies find

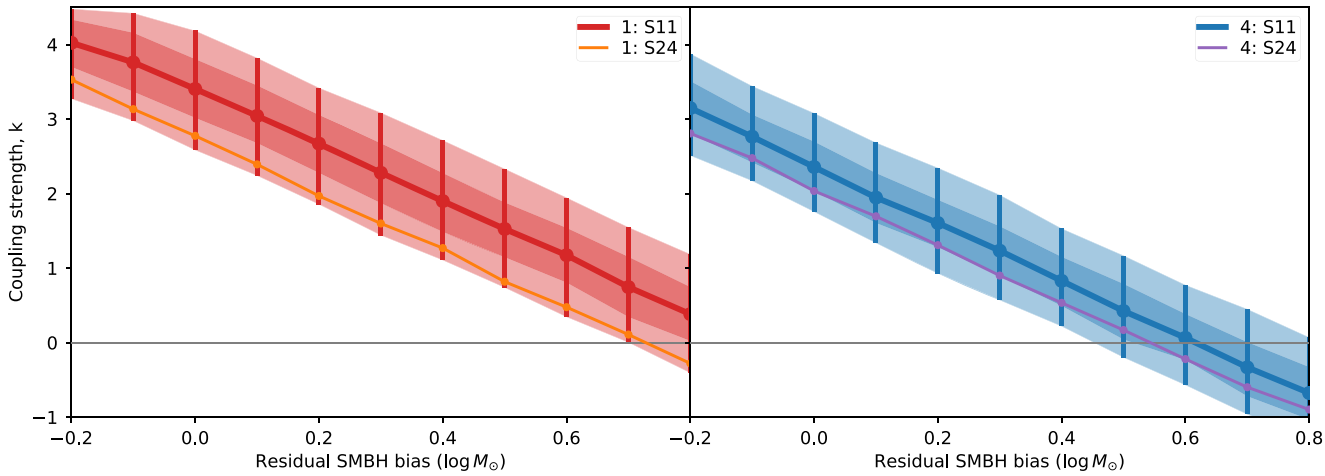


Figure 4. As Figure 3, but replacing an SMBH mass offset with the strength, k, of cosmological coupling (Equation (16)) needed to align the high- and low-redshift relations.

$2 \lesssim f_{\rm vir} \lesssim 4$ (F. Shankar et al. 2019; A. K. Mandal et al. 2021; S24), which would lower our high-redshift SMBH masses by ∼0.3 dex. Other studies argue for $f_{\rm vir} \sim 1$–20, and that it can depend on the accretion rate (H. T. Liu et al. 2022, 2024). If true then $\langle f_{\rm vir} \rangle \sim 4$ may be reasonable, but a dependence on accretion rate may affect the slope and intercept of the intrinsic $M_\bullet$–M_* relation, akin to the effect of different SEV calibrators. Second is $p_{\rm act}$. We have assumed a loose range of $0.0001 < p_{\rm act} < 0.2$ over all SMBH masses. It is however possible that a tighter range, or one that depends on SMBH mass, could alter the values of a, b, and σ_t that give acceptable observed relations.

A thorough investigation of these dependencies would require a much larger sample. We argue though that any study of the $M_\bullet$–M_* relation for AGN requires a well-matched measure of the SMF, BHMF, and ERDF to minimize bias. Even then, residual uncertainty from the choice of SEV calibrator, $f_{\rm vir}$, and $p_{\rm act}$, will lead to a systematic uncertainty in the $M_\bullet$–M_* relation of ∼0.3–0.5 dex. The $M_\bullet$–M_* plane is thus a challenging arena to study galaxy assembly with redshift. The $M_\bullet$–stellar velocity dispersion plane may be more fundamental, and less prone to bias (F. Shankar et al. 2017).

5.2. Early-type Galaxy Assembly over 0 < z < 1

If our high-redshift sample are ETGs emerging onto the red sequence, then our high- and low-redshift $M_\bullet$–M_* relations can diagnose the processes that affect ETG assembly between $z \sim 1$ and $z \sim 0$. From Figure 5 our high-redshift relation lies below our low-redshift relation but above the relation for $z \sim 0$ AGN (albeit for lower-luminosity AGN in all host types). We here examine the implications of these offsets, and the possible further bias corrections (Section 5.2.1) and physical mass changes (Section 5.2.2) that may align them.

5.2.1. Alignment with Bias Corrections

Depending on parameter choices, ∼0.4–1 dex of bias corrections, beyond those we applied, are required to align the high-redshift intrinsic relation with the low-redshift relation. A plausible origin for some of this is dynamical selection bias in the low-redshift sample. From F. Shankar et al. (2016), dynamical selection bias much above 0.4 dex is unlikely in the stellar mass range of our sample, but a bias of up to 0.4 dex is feasible. There is support for this idea from studies of the redshift evolution of scaling relations by integrating along curves of M_* (G. Yang et al. 2018; R. Carraro et al. 2020; F. Shankar et al. 2020b), which find that, with dynamical selection bias in low-redshift objects, the local $M_\bullet$–M_* relation can be reconciled with high-redshift measurements. Dynamical selection bias in low-redshift ETGs has, however, not been directly confirmed.

Another selection bias that may align the high- and low-redshift relations is "downsizing," in which ETGs with relatively more massive SMBHs complete their assembly earlier. In this scenario, our $z \sim 0.8$ ETGs represent those that

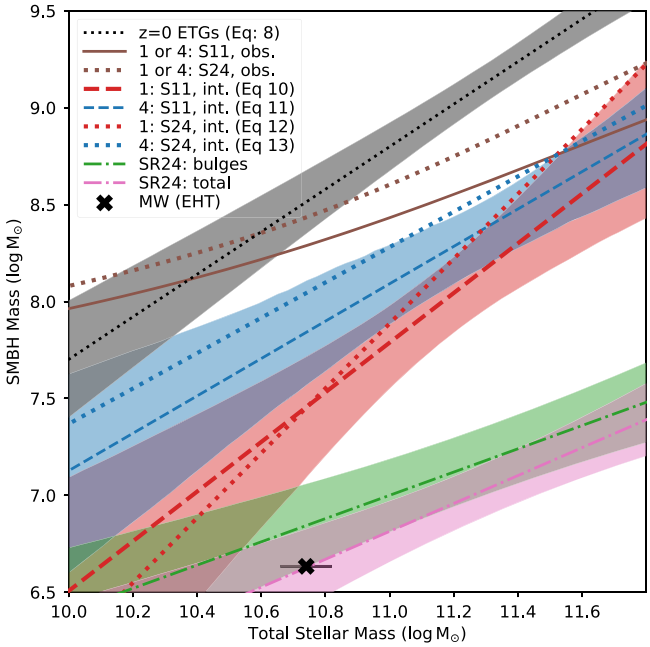


Figure 5. Our low- and high-redshift relations compared to the $z \sim 0$ AGN relations from M. R. Sturm & A. E. Reines (2024, who use the A. E. Reines et al. 2013 SEV relation). Also shown is the Milky Way with SMBH mass from the Event Horizon Telescope Collaboration et al. (2022). We do not plot other literature relations (e.g., J. E. Greene et al. 2016; M. C. Bentz & E. Manne-Nicholas 2018; Z. Schutte et al. 2019; V. N. Bennert et al. 2021; J. I. H. Li et al. 2023) as their uncertainties are significant, but in general they are consistent with ours.

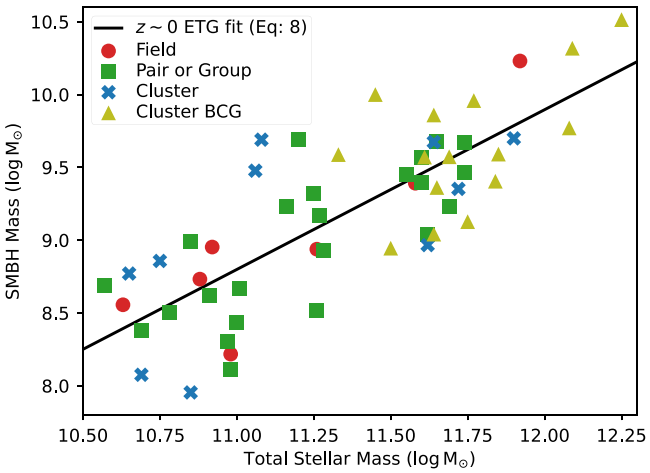


Figure 6. As Figure 1, left, with the sample classified by their local environment. The sample are all at $z < 2$, so residual redshift bias will be insignificant.

complete their assembly relatively late, and hence have undermassive SMBHs. Support for this idea comes from studies of high-redshift starbursts (L. Wang et al. 2013; A. Wilkinson et al. 2017) and of overmassive SMBHs at $z \gtrsim 2$ (e.g., L. J. Furtak et al. 2024; R. Maiolino et al. 2024), though these studies do not restrict to ETG hosts. If interpreted this way, our results strongly favor downsizing as they place the $z \sim 0.8$ AGN in ETG hosts between our low-redshift and $z > 1$ $M_\bullet$–M_* relations. A decisive test of this possibility requires knowledge of the stellar mass assembly histories of our sample, which only a few have (R. M. McDermid et al. 2015). We can however perform a basic check by first noting that ETGs assemble earlier in denser environments (D. Thomas et al. 2005). If low-redshift ETGs with higher $M_\bullet/M_*$ ratios assembled earlier, then they may reside in denser environments. Our low-redshift sample lacks homogeneous measures of environment, so we classify them as isolated, group, cluster, or brightest cluster galaxy, based on the information in the NASA/IPAC Extragalactic Database, and plot them in the $M_\bullet$–M_* plane (Figure 6). There is no clear trend for systems with relatively more massive SMBHs to prefer denser environments. This test is not robust, but it does suggest that any signatures of downsizing in ETG assembly are subtle.

A further possible bias is if the high-redshift hosts are contaminated by dusty lenticular galaxies. The possibility of such a population has been raised by A. W. Graham (2024). Such a population, with on average smaller SMBHs, could explain our result. Based on the selection of the AGN to have low reddening, we do not believe this is likely, but we cannot exclude it.

Finally, there are two measurement biases that could help align our relations. First is residual stellar mass measurement bias. With the S24 calibrator, the required stellar mass bias would be ∼0.4 dex. This seems only barely plausible, for the reasons given in Section 3.1.2. It cannot be discounted though. The high-redshift host SEDs must be resolved against a much brighter AGN, meaning that a significant overestimate in M_* is possible. We lack the data to test this. However, if the stellar masses of the high-redshift sample are corrected downward, then this will increase the SMBH selection bias in the sample. For example, a 0.3 dex downward M_* correction would increase the SMBH selection bias by ∼0.2 dex. Stellar mass measurement bias thus seems an implausible route to aligning the high- and low-redshift relations. Second, our high-redshift host classifications may be incorrect. If they are contaminated by disk hosts, then the offset we observe between the high- and low-redshift relations could signpost an episode of preferential SMBH growth in a major merger (e.g., D. Farrah et al. 2016, 2022). Testing this possibility would require spatially resolved imaging of the quasar hosts, which we do not have.

5.2.2. Alignment with Mass Changes

Either stellar mass loss or preferential SMBH mass growth between $z \sim 0.8$ and $z = 0$ ($\Delta t \sim 7$ Gyr) could align the high- and low-redshift relations. Stellar mass loss is implausible, since processes such as cluster infall cannot remove enough stellar mass to align the relations (F23, and references therein). This leaves preferential SMBH mass growth. Of order $5 \times 10^8\ M_\odot$ of SMBH growth is required to align the relations, assuming no increase in stellar mass. Four routes could achieve this: "slow and steady" accretion, rapid accretion as an AGN, SMBH mergers, or cosmological coupling.

For slow and steady accretion to align the relations, the average accretion rate is $\dot{M}_\bullet \sim 7 \times 10^{-2}\ M_\odot\ \mathrm{yr}^{-1}$. While there are routes that could supply gas at such rates (e.g., A. C. Fabian et al. 2024; L. R. Ivey et al. 2024), and the typical $\dot{M}_\bullet/\dot{M}_*$ ratio in ETGs (M. McDonald et al. 2021) gives a plausible SFR, the accretion rate itself is typical of AGN. This seems unlikely. Brief, rapid accretion is more viable, since high accretion rates can be triggered in gas-rich mergers, but would require most ETGs to go through at least one such merger between $z \sim 0.8$ and $z = 0$. The merger rate required seems in tension with recent predictions (e.g., J. A. O'Leary et al. 2021).

For SMBH–SMBH mergers to align the relations then, if exotic possibilities (W. H. Press & S. A. Teukolsky 1972) are neglected, the $M_\bullet/M_*$ ratio in the "other" galaxy must be at least that seen in local ETGs. This is in principle plausible, as ultracompact galaxies with overmassive SMBHs have been found in the haloes of ETGs (A. C. Seth 2014; K. T. Voggel et al. 2019). However, to increase the SMBH masses by at least 0.3 dex relative to the stellar mass would require tens of such mergers.

Finally, cosmologically coupled BH growth could align the high- and low-redshift relations. This requires $k \simeq 1$–3, depending on the choices of SMF, BHMF, and ERDF parameters, and SEV calibrator. Values in this range are plausible: $k = 3$ has been proposed to link BHs with dark energy (D. Farrah et al. 2023a), and $k = 1$ has a known exact solution (M. Cadoni et al. 2023a). Neither value is, however, independently preferred. M. Lacy et al. (2024) have shown that, with conventional assumptions about the local SMBH mass density (e.g., A. W. Graham & S. P. Driver 2007), $k < 2$ is required, but with the SMBH mass density proposed by G. Agazie et al. (2023) then $k > 2$ may be required. Some studies of stellar-mass BHs are consistent with $k \sim 3$ (S.-J. Gao & X.-D. Li 2023) but others find that $k \gtrsim 2$ may require the zero-age masses of BHs formed through stellar collapse to lie below the Tolman–Oppenheimer–Volkov (TOV) limit[22] (R. Andrae & K. El-Badry 2023; S. Ghodla et al. 2023; C. L. Rodriguez 2023; L. Amendola et al. 2024; E. Mlinar & T. Zwitter 2024). Our study cannot resolve this controversy,

[22] This is possible, since the TOV limit is only a lower bound on BH mass if BHs have trapping surfaces, which cosmologically coupled BHs may not have. To date though, no BH below the TOV limit has been found.

but does show that $k > 0$ is viable from observations of galaxy scaling relations.

6. Conclusions

We have studied the $M_\bullet$–M_* relation in two samples of ETGs with $M_* > 10^{10.5}$ $M_\odot$. First, quiescent, morphologically selected ETGs at $z < 0.2$ with SMBH masses from dynamical modeling. Second, AGN ($L_{\rm bol} \geqslant 10^{45.5}$ erg s^{-1}) in ETGs at $z \sim 0.8$, selected through SED fitting, with SMBH masses from the virial method. We compare their $M_\bullet$–M_* relations to constrain the assembly histories of ETGs. We find the following conclusions:

1. For the $z < 0.2$ sample the observed mean relation is $\log M_\bullet = 8.80^{+0.12}_{-0.12} + 1.10^{+0.21}_{-0.21}(\log M_* - 11)$, with scatter $\sigma = 0.37^{+0.08}_{-0.06}$. This is in line with prior work, and suggests a tight intrinsic relation. For the $z \sim 0.8$ AGN, we adopt the S11 virial relation, $f_{\rm vir} = 4.3$, and correct for selection bias. The intrinsic mean relation is then $\log M_\bullet = 7.80^{+0.18}_{-0.24} + 1.25^{+0.68}_{-0.47}(\log M_* - 11)$ with $\sigma = 0.24^{+0.18}_{-0.38}$. This relation lies below our $z < 0.2$ relation in SMBH mass by $\sim$1 dex, but has a consistent slope. It lies above the $M_\bullet$–M_* relation for local AGN by $\sim$0.5 dex.
2. The $z \sim 0.8$ intrinsic $M_\bullet$–M_* relation depends on the SMF and active BHMF and ERDF used to calculate the selection bias, the virial relation, the virial factor, and the active fraction. Different choices of these variables can alter the intercept of the intrinsic relation by up to $\sim$0.6 dex, and the slope by up to $\sim$0.4 dex. These changes can arise by altering the SMF, BHMF, and ERDF by amounts comparable to changes in them seen in redshift intervals of $\Delta z \sim 0.5$. We further show that the SMF and BHMF/ERDF cannot be constrained using samples of order 10^2 objects in the $M_\bullet$–M_* plane. Since the virial relation, virial factor, and active fraction are also challenging to constrain with such samples, these variables act as systematic biases in any study of the $M_\bullet$–M_* relation in AGN.
3. Reasonable choices of the model variables gives an SMBH mass offset between the $z < 0.2$ and $z \sim 0.8$ relations of $\sim$0.4–1 dex. We explore ways to align the two $M_\bullet$–M_* relations. Dynamical selection bias in the $z < 0.2$ sample could account for some, possibly all, of the offset. Another possibility is "downsizing:" ETGs with relatively more massive SMBHs assemble at higher redshifts. Other possibilities that could align the relations include brief, rapid accretion events, contamination by disk or dusty lenticular hosts, or cosmologically coupled SMBH mass growth.
4. Our results demonstrate the importance of several avenues of study for using the $M_\bullet$–M_* plane as a diagnostic tool. These include the redshift, environment, and morphology dependence of the SMF, BHMF, and ERDF, the calibration of stellar and virial SMBH masses, and the possible model dependence of the virial factor and active fraction.

Acknowledgments

We thank the referee for a very helpful report. We thank Michael Rowan-Robinson, River, and John Petty for helpful discussions. F.S. acknowledges partial support from the EU H2020-MSCA-ITN-2019 Project 860744 "BiD4BESt: Big Data applications for black hole Evolution STudies" (Coordinator: F. Shankar). R.A.W. acknowledges support from NASA JWST Interdisciplinary Scientist grants NAG5-12460, NNX14AN10G, and 80NSSC18K0200 from GSFC. J.A. acknowledges financial support from the Science and Technology Foundation (FCT, Portugal) through research grants PTDC/FIS-AST/29245/2017, UIDB/04434/2020 (doi:10.54499/UIDB/04434/2020) and UIDP/04434/2020 (doi:10.54499/UIDP/04434/2020).

ORCID iDs

D. Farrah https://orcid.org/0000-0003-1748-2010
A. Engholm https://orcid.org/0000-0001-6970-7782
E. Hatziminaoglou https://orcid.org/0000-0003-0917-9636
S. Petty https://orcid.org/0000-0003-0624-3276
F. Shankar https://orcid.org/0000-0001-8973-5051
A. Efstathiou https://orcid.org/0000-0002-2612-4840
K. Ejercito https://orcid.org/0009-0002-6970-5247
K. Jones https://orcid.org/0000-0001-7685-158X
M. Lacy https://orcid.org/0000-0002-3032-1783
C. Lonsdale https://orcid.org/0000-0003-0898-406X
C. Pearson https://orcid.org/0000-0001-6139-649X
G. Tarlé https://orcid.org/0000-0003-1704-0781
R. A. Windhorst https://orcid.org/0000-0001-8156-6281
J. Afonso https://orcid.org/0000-0002-9149-2973
D. L. Clements https://orcid.org/0000-0002-9548-5033
K. S. Croker https://orcid.org/0000-0002-6917-0214
L. K. Pitchford https://orcid.org/0000-0002-5206-5880

References

Agazie, G., Anumarlapudi, A., Archibald, A. M., et al. 2023, ApJL, 952, L37
Amendola, L., Rodrigues, D. C., Kumar, S., & Quartin, M. 2024, MNRAS, 528, 2377
Andrae, R., & El-Badry, K. 2023, A&A, 673, L10
Aversa, R., Lapi, A., de Zotti, G., Shankar, F., & Danese, L. 2015, ApJ, 810, 74
Barrows, R. S., Comerford, J. M., Stern, D., & Assef, R. J. 2021, ApJ, 922, 179
Bennert, V. N., Treu, T., Ding, X., et al. 2021, ApJ, 921, 36
Bentz, M. C., & Manne-Nicholas, E. 2018, ApJ, 864, 146
Boizelle, B. D., Barth, A. J., Walsh, J. L., et al. 2019, ApJ, 881, 10
Cadoni, M., Murgia, R., Pitzalis, M., & Sanna, A. P. 2023a, JCAP, 2024, 026
Cadoni, M., Sanna, A. P., Pitzalis, M., et al. 2023b, JCAP, 2023, 007
Carraro, R., Rodighiero, G., Cassata, P., et al. 2020, A&A, 642, A65
Cloonan, A. P., Khullar, G., Napier, K. A., et al. 2024, arXiv:2408.03379
Cohn, J. H., Walsh, J. L., Boizelle, B. D., et al. 2021, ApJ, 919, 77
Croker, K. S., Nishimura, K. A., & Farrah, D. 2020, ApJ, 889, 115
Croker, K. S., & Weiner, J. L. 2019, ApJ, 882, 19
Croker, K. S., Weiner, J. L., & Farrah, D. 2022, PhRvD, 105, 084042
Decarli, R., Falomo, R., Treves, A., et al. 2010, MNRAS, 402, 2453
de Nicola, S., Thomas, J., Saglia, R. P., et al. 2024, MNRAS, 530, 1035
Delvecchio, I., Daddi, E., Aird, J., et al. 2020, ApJ, 892, 17
Ding, X., Silverman, J., Treu, T., et al. 2020, ApJ, 888, 37
Event Horizon Telescope Collaboration, Akiyama, K., Alberdi, A., et al. 2022, ApJL, 930, L15
Fabian, A. C. 2012, ARA&A, 50, 455
Fabian, A. C., Sanders, J. S., Ferland, G. J., et al. 2024, MNRAS, 531, 267
Faraoni, V., & Jacques, A. 2007, PhRvD, 76, 063510
Faraoni, V., & Rinaldi, M. 2024, PhRvD, 110, 063553
Farrah, D., Baloković, M., Stern, D., et al. 2016, ApJ, 831, 76
Farrah, D., Efstathiou, A., Afonso, J., et al. 2022, MNRAS, 513, 4770
Farrah, D., Croker, K. S., Zevin, M., et al. 2023a, ApJL, 944, L31
Farrah, D., Petty, S., Croker, K. S., et al. 2023b, ApJ, 943, 133
Ferrarese, L., & Merritt, D. 2000, ApJL, 539, L9
Furtak, L. J., Labbé, I., Zitrin, A., et al. 2024, Natur, 628, 57
Gao, S.-J., & Li, X.-D. 2023, ApJ, 956, 128
Gebhardt, K., Bender, R., Bower, G., et al. 2000, ApJL, 539, L13
Ghodla, S., Easther, R., Briel, M. M., & Eldridge, J. J. 2023, OJAp, 6, 25
Graham, A. W. 2024, MNRAS, 531, 230

Graham, A. W., & Driver, S. P. 2007, MNRAS, 380, L15
Greene, J. E., Seth, A., Kim, M., et al. 2016, ApJL, 826, L32
Greene, J. E., Veale, M., Ma, C.-P., et al. 2019, ApJ, 874, 66
Habouzit, M., Li, Y., Somerville, R. S., et al. 2021, MNRAS, 503, 1940
Hirschmann, M., Khochfar, S., Burkert, A., et al. 2010, MNRAS, 407, 1016
Ivey, L. R., Fabian, A. C., Sanders, J. S., et al. 2024, MNRAS, 535, 2697
Kormendy, J., & Ho, L. C. 2013, ARA&A, 51, 511
Kroupa, P. 2002, Sci, 295, 82
Lacy, M., Engholm, A., Farrah, D., & Ejercito, K. 2024, ApJL, 961, L33
Le, H. A. N., Woo, J.-H., & Xue, Y. 2020, ApJ, 901, 35
Li, J., Silverman, J. D., Ding, X., et al. 2021a, ApJ, 922, 142
Li, J. I. H., Shen, Y., Ho, L. C., et al. 2021b, ApJ, 906, 103
Li, J. I. H., Shen, Y., Ho, L. C., et al. 2023, ApJ, 954, 173
Liu, H. T., Feng, H.-C., Li, S.-S., & Bai, J. M. 2022, ApJ, 928, 60
Liu, H. T., Feng, H.-C., Li, S.-S., Bai, J. M., & Li, H. Z. 2024, ApJ, 963, 30
Maiolino, R., Scholtz, J., Witstok, J., et al. 2024, Natur, 627, 59
Mandal, A. K., Rakshit, S., Stalin, C. S., et al. 2021, MNRAS, 502, 2140
McConnell, N. J., & Ma, C.-P. 2013, ApJ, 764, 184
McDermid, R. M., Alatalo, K., Blitz, L., et al. 2015, MNRAS, 448, 3484
McDonald, M., McNamara, B. R., Calzadilla, M. S., et al. 2021, ApJ, 908, 85
McLeod, D. J., McLure, R. J., Dunlop, J. S., et al. 2021, MNRAS, 503, 4413
Merloni, A., Bongiorno, A., Bolzonella, M., et al. 2010, ApJ, 708, 137
Mejía-Restrepo, J. E., Lira, P., Netzer, H., Trakhtenbrot, B., & Capellupo, D. M. 2018, NatAs, 2, 63
Mlinar, E., & Zwitter, T. 2024, MNRAS, 528, 3000
Ni, Q., Brandt, W. N., Yang, G., et al. 2021, MNRAS, 500, 4989
Nightingale, J. W., Smith, R. J., He, Q., et al. 2023, MNRAS, 521, 3298
O'Leary, J. A., Moster, B. P., Naab, T., & Somerville, R. S. 2021, MNRAS, 501, 3215
Press, W. H., & Teukolsky, S. A. 1972, Natur, 238, 211
Rakshit, S., Stalin, C. S., & Kotilainen, J. 2020, ApJS, 249, 17
Reines, A. E., Greene, J. E., & Geha, M. 2013, ApJ, 775, 116
Reines, A. E., & Volonteri, M. 2015, ApJ, 813, 82
Rodriguez, C. L. 2023, ApJL, 947, L12
Saglia, R., Mehrgan, K., & de Nicola, S. 2024, A&A, 692, A124
Sahu, N., Graham, A. W., & Davis, B. L. 2019, ApJ, 876, 155
Schramm, M., & Silverman, J. D. 2013, ApJ, 767, 13
Schulze, A., Bongiorno, A., Gavignaud, I., et al. 2015, MNRAS, 447, 2085
Schulze, A., & Wisotzki, L. 2011, A&A, 535, A87
Schutte, Z., Reines, A. E., & Greene, J. E. 2019, ApJ, 887, 245
Seth, A. C., van den Bosch, R., Mieske, S., et al. 2014, Natur, 513, 398
Shankar, F., Allevato, V., Bernardi, M., et al. 2020a, NatAs, 4, 282
Shankar, F., Bernardi, M., & Sheth, R. K. 2017, MNRAS, 466, 4029
Shankar, F., Bernardi, M., Sheth, R. K., et al. 2016, MNRAS, 460, 3119
Shankar, F., Bernardi, M., Richardson, K., et al. 2019, MNRAS, 485, 1278
Shankar, F., Weinberg, D. H., Marsden, C., et al. 2020b, MNRAS, 493, 1500
Shen, Y., Greene, J. E., Strauss, M. A., Richards, G. T., & Schneider, D. P. 2008, ApJ, 680, 169
Shen, Y., Grier, C. J., Horne, K., et al. 2024, ApJS, 272, 26
Shen, Y., Richards, G. T., Strauss, M. A., et al. 2011, ApJS, 194, 45
Sijacki, D., Vogelsberger, M., Genel, S., et al. 2015, MNRAS, 452, 575
Silk, J. 2013, ApJ, 772, 112
Speagle, J. S. 2020, MNRAS, 493, 3132
Sturm, M. R., & Reines, A. E. 2024, ApJ, 971, 173
Suh, H., Civano, F., Trakhtenbrot, B., et al. 2020, ApJ, 889, 32
Tanaka, T. S., Silverman, J. D., Ding, X., et al. 2025, ApJ, 979, 215
Thater, S., Krajnović, D., Cappellari, M., et al. 2019, A&A, 625, A62
Thater, S., Krajnović, D., Weilbacher, P. M., et al. 2022, MNRAS, 509, 5416
Thater, S., Lyubenova, M., Fahrion, K., et al. 2023, A&A, 675, A18
Thomas, D., Maraston, C., Bender, R., & Mendes de Oliveira, C. 2005, ApJ, 621, 673
Ueda, Y., Hatsukade, B., Kohno, K., et al. 2018, ApJ, 853, 24
Voggel, K. T., Seth, A. C., Baumgardt, H., et al. 2019, ApJ, 871, 159
Wang, L., Farrah, D., Oliver, S. J., et al. 2013, MNRAS, 431, 648
Waters, T. K., Gültekin, K., Gebhardt, K., Nagar, N., & Ávila, V. 2024, ApJ, 971, 149
Watkins, A. E., Salo, H., Laurikainen, E., et al. 2022, A&A, 660, A69
Weaver, J. R., Davidzon, I., Toft, S., et al. 2023, A&A, 677, A184
Weigel, A. K., Schawinski, K., & Bruderer, C. 2016, MNRAS, 459, 2150
Weinberger, R., Springel, V., Hernquist, L., et al. 2017, MNRAS, 465, 3291
Wilkinson, A., Almaini, O., Chen, C.-C., et al. 2017, MNRAS, 464, 1380
Wu, Q., & Shen, Y. 2022, ApJS, 263, 42
Yang, G., Brandt, W. N., Vito, F., et al. 2018, MNRAS, 475, 1887
Zhang, Y., Ouchi, M., Gebhardt, K., et al. 2023, ApJ, 948, 103
Zhao, Y., Ho, L. C., Shangguan, J., et al. 2021, ApJ, 911, 94
Zuo, W., Wu, X.-B., Fan, X., et al. 2015, ApJ, 799, 189